nature communications

Article

https://doi.org/10.1038/s41467-026-75200-8

Structural and spectral adaptation of the seagrass *Posidonia oceanica* photosystem I to seabed light

Received: 11 January 2026

Accepted: 24 June 2026

Published online: 16 July 2026

Check for updates

Antonello Amelii[1,7], Stefano Capaldi[1,2,7], Mattia Russo[3], Zeno Guardini[1], Gennaro Sanità[4], Emanuela Esposito[4], Irene Olivé[5], Margherita Maiuri[3], Luca Dall'Osto[1], Giulio Cerullo[3,6], Gabriele Procaccini[5] & Roberto Bassi[1,5,6]

Seagrasses are marine angiosperms re-adapted to underwater life, forming productive ecosystems and long-term carbon sinks. *Posidonia oceanica* thrives up to 50 m depth, where light is scarce and spectrally shifted; yet, the molecular basis of its photosynthetic adaptation remains unclear. Here, we report that *P. oceanica* genetically adapts for highly efficient photon use under dim light by enhancing photosystem antenna size and reducing exciton trapping time. We determine the structures of *P. oceanica* PSI supercomplexes by cryo-electron microscopy, revealing an expanded antenna system composed of PSI-LHCI, a trimeric phospho-LHCII, and an additional LHCI heterodimer. Low-energy chlorophyll forms associated with LHCI are lost. Ultrafast spectroscopy shows that this loss correlates with faster exciton trapping, which compensates for antenna expansion and enhances light-use efficiency under dim light. We identify key residues responsible for the loss of low-energy forms. Reversion to land-plant ortholog sequences restores red-shifted emission, providing strategies to enhance light-use efficiency in crops.

The colonization of land by plants, which evolved from a green algal ancestor, was a transformative event in Earth's history, boosting atmospheric oxygen, driving soil formation, reshaping climate and sedimentation, and enabling the development of complex terrestrial ecosystems[1]. A subset of monocots later returned to the sea independently between 70–100 million years ago, giving rise to ~80 flowering seagrass species distributed across temperate and tropical coasts. Seagrass meadows are estimated to cover 0.6–1.6 M km² of seafloor[2], ranking among the most productive ecosystems on Earth[3]. They efficiently sequester CO_2 through photosynthesis and store organic matter in sediments for millennia[4]. Despite occupying just 0.1% of the ocean surface, seagrasses bury an estimated 27–44 gigatons of organic carbon per year globally, up to 40 times more efficiently than forest soils[5]. Their genomes include 20,000–28,000 genes fewer than terrestrial plants, reflecting simplification linked to aquatic life[6]. Yet, seagrasses face strong environmental constraints: water rapidly attenuates light, especially red and far-red wavelengths within a few meters, leaving a narrow blue-green spectrum[7]. Additional attenuation arises from canopy self-shading and epiphytic growth on leaves[8]. This effect is homologous, yet opposite, to that in land canopies, where upper leaves enrich far-red light in the understory, limiting photosynthesis[9].

Oxygenic photosynthesis, the process that converts light into chemical energy, sustains both terrestrial and marine ecosystems. It is

[1]Laboratory of Photosynthesis and Bioenergy, Department of Biotechnology, University of Verona; Strada Le Grazie 15, Verona, Italy. [2]Biocristallography Laboratory, Department of Biotechnology, University of Verona; Strada Le Grazie 15, Verona, Italy. [3]Department of Physics, Politecnico di Milano, Piazza L. da Vinci 32, Milano, Italy. [4]Eye Lab, Institute of Applied Sciences and Intelligent Systems Unit of Naples, National Research Council; Via Campi Flegrei 34, Naples, Italy. [5]Stazione Zoologica Anton Dohrn Napoli; Villa Comunale, Naples, Italy. [6]Accademia Nazionale dei Lincei; Palazzo Corsini, Via della Lungara 10, Rome, Italy. [7]These authors contributed equally: Antonello Amelii, Stefano Capaldi. e-mail: roberto.bassi@univr.it

driven by Photosystem II (PSII, P680) and Photosystem I (PSI, P700), multi-pigment protein complexes embedded in the thylakoid membrane. They drive electron flow to generate ATP and NADPH for CO_2 fixation. Each photosystem has a core reaction center (RC), where charge separation takes place, surrounded by light-harvesting complexes (LHCs)-LHCII for PSII, LHCI for PSI-which harvest photons and transfer excitation energy to the core[10,11]. Efficient electron transport requires balanced excitation of PSI and PSII, maintained through dynamic regulation of antenna proteins, which optimize light harvesting and photoprotection in different light environments[11–13]. Underwater, light intensity decreases with depth, and blue-green wavelengths dominate, which are preferentially absorbed by chlorophyll (Chl) *b*/*c* and carotenoids abundant in the PSII antenna subunits, thereby enhancing its photon absorption capacity relative to PSI-LHCI. To thrive in marine light conditions, eukaryotic aquatic organisms have evolved enlarged PSI antenna systems with multiple additional subunits bound to the core, increasing the absorption cross-section[14–16].

Posidonia oceanica (Po), an endemic seagrass species of the Mediterranean Sea, exhibits high productivity and contributes substantially to coastal ecosystems. It forms extensive meadows from shallow waters to 50 m depths, covering ~25% of Mediterranean coastal seabeds[17], with some meadows up to 80,000 years old[18]. These meadows stabilize sediments, provide habitats for marine life, and sequester ~270 t carbon/hectare/year[19]. So far, most *P. oceanica* studies have focused on ecology, genomics, and transcriptomics[6,20], while structural and functional insights into photosystems are essential to identify the photosynthetic molecular adaptations[21].

Here, we report on the photosynthetic adaptations that enable *P. oceanica* to thrive underwater, focusing on PSI, whose excitation becomes limited with depth. Using single-particle cryo-electron microscopy (Cryo-EM), we solve the structures of two supercomplexes: PSI-LHCI at 2.83 Å resolution, and a larger PSI-LHCI-LHCII (hereafter renamed PSI-LHCI-mega) at 3.31 Å resolution, revealing an expanded antenna architecture and subunit interactions. Pigment mapping enables the identification of excitation energy transfer (EET) pathways, and two-dimensional electronic spectroscopy (2DES) experimentally quantifies their dynamics, revealing how the loss of low-energy Chl forms modulates EET dynamics while maintaining high efficiency. Integrating structural and functional data, we pinpoint amino acid substitutions responsible for this spectral shift and validate their role using recombinant *Po*Lhca4 variants that restore low-energy Chl forms. Overall, these findings reveal structural and functional adaptations that enable *P. oceanica* to optimize photosynthesis under marine light regimes, offer insights into PSI evolution during the land-to-sea transition, and provide a framework for engineering LHCs to tune their light absorption properties.

Results

Characterization of *P. oceanica* photosynthetic function

P. oceanica plants were collected by SCUBA diving at −4 mt and −22 mt depth in Lacco Ameno meadows (Ischia Island, Gulf of Naples, Italy) (Supplementary Fig. 1a, b). Photosynthetic activity, measured as the relative electron transport rate of PSII (ETR-II), showed a near-linear increase in efficiency up to 50–60 µmol photons s^{-1} m^{-2}, peaking at ~90 before declining by ~40% at 900. In contrast, *Arabidopsis thaliana* (*At*) and *Zea mays* (*Zm*) saturated at ~270 and ~400 µmol photons s^{-1} m^{-2}, respectively, maintaining stable ETR-II values up to 900 (Fig. 1a). These findings indicate that *P. oceanica* is optimized for exploiting low-light conditions irrespective of the light availability in a specific growth site, consistent with similar ETR-II responses at different depths. Consistently, non-photochemical quenching (NPQ), an index of excess energy dissipation as heat, was strongly reduced in *P. oceanica* compared to land plants (Supplementary Fig. 2a), with lower amplitude in depths[21]. Although PSII quantum efficiency was similar across species (Supplementary Fig. 2b), both PSII and PSI functional cross-sections were larger in *P. oceanica*, increasing with growth depth, from ~41% larger at 4 m to ~50% at 22 m for PSII, and from ~39% to ~49% for PSI compared to *A. thaliana* (Fig. 1b, c), consistent with the presence of a PSI-LHCI-mega complex (Supplementary Fig. 2c)[21,22]. Due to strong red-light attenuation underwater (Supplementary Fig. 1c), PSI/PSII excitation balance would typically rely on State 1-State 2 transitions (ST1-2)[23]. However, *P. oceanica* exhibited a ~four-fold lower ST amplitude than land plants (Fig. 1d), further reduced at −22 m, suggesting that reversible LHCII phosphorylation plays only a minor role in acclimation. Overall, these results suggest that *P. oceanica* maintains photosynthetic efficiency in low light primarily through constitutive structural adaptations, including enlarged antenna systems.

To examine the molecular basis for *P. oceanica*'s enlarged antenna size and dim light adaptation, we compared its pigment-protein complexes with those of land plants. Solubilized thylakoid membranes were fractionated by sucrose density gradient ultracentrifugation, resolving five major pigment-protein bands corresponding to free pigments, monomeric and trimeric LHC, monomeric PSII core, and PSI-LHCI (Fig. 1e)[24]. In *P. oceanica*, LHCII absorption spectra exhibited enhanced bands at 656 nm (Q_y) and in the Soret region (462–483 nm), suggesting higher Chl *b* content compared to land plants (Supplementary Fig. 3a). Pigment analysis confirmed a lower Chl *a*/*b* ratio in *Po*LHCII compared to *A. thaliana* (Supplementary Fig. 3b)[21]. Notably, *P. oceanica* displayed an additional high-molecular-weight band (B7; Fig. 1e), which, compared with the B6, contained higher Chl *b* and xanthophylls, reflected in enhanced absorption at 650 and 460–480 nm, while retaining a major Q_y transition at 680 nm (Supplementary Fig. 3c, g). This band corresponds to a PSI-LHCI supercomplex (Supplementary Fig. 3d, e). Low-temperature fluorescence spectrum (Fig. 1f) revealed that the B6 only emitted at 722 nm, whereas B7 showed an additional component at 680 nm, consistent with the presence of trimeric LHCII, supported by high Chl *b* and neoxanthin levels (Supplementary Fig. 3c, g) and by SDS-PAGE profiles (Supplementary Fig. 3e). Both, *P. oceanica* PSI supercomplexes emission at 722 nm was blue-shifted relative to the 732–736 nm peaks of land plants (Fig. 1f), which arise from low-energy Chl forms in LHCI subunits[25,26], showing the latter are lost in the seagrass during the land-to-sea transition. Immunoblotting confirmed that B6 contained only PSI components, whereas B7 also included Lhcb1 and phosphorylated Lhcb2, which are LHCII subunits (Supplementary Fig. 3f).

These findings reveal unique traits of *P. oceanica* antenna system, featuring: trimeric LHCII bound to PSI, modified LHCI subunits, and altered energy profiles adapted to dim, red-depleted underwater light.

Structures of *P. oceanica* PSI-LHCI and PSI-LHCI-mega complexes

To uncover the structural and molecular basis of *P. oceanica* adaptation, we determined the structures of PSI supercomplexes by purifying B6 and B7 (Fig. 1e) and analyzed them by Cryo-EM (Supplementary Figs. 4, 5). B6 contained a canonical PSI-LHCI complex, with a cheese-slice-shaped PSI core and a peripheral half-moon LHCI belt of four subunits (Fig. 2a, b), consistent with earlier reports[26–29]. The final reconstruction achieved an overall resolution of 2.83 Å (Supplementary Fig. 6a–c), allowing for the accurate modeling of the 12 core subunits (PsaA-PsaL) and 4 LHCI subunits (Lhca1-4), except for the stromal subunit PsaN (Supplementary Fig. 7a, b). The final PSI-LHCI model comprised 16 protein chains, 194 pigments (143 Chl *a*, 12 Chl *b*, 30 β-carotenes, and 9 xanthophylls), 3 Fe_4S_4 clusters, and 20 lipids (Fig. 2c, Supplementary Fig. 8a and Supplementary Table 1). Overall, the architecture and pigment arrangement of *Po*PSI-LHCI resembled land plant complexes[26,29–32], but appeared more relaxed, with slightly increased inter-subunit distances. Superposition with other plant PSI structures[26,31] (aligned on Lhca1) revealed a displacement of ~3–9.5 Å in the position of the third transmembrane helix of Lhca3

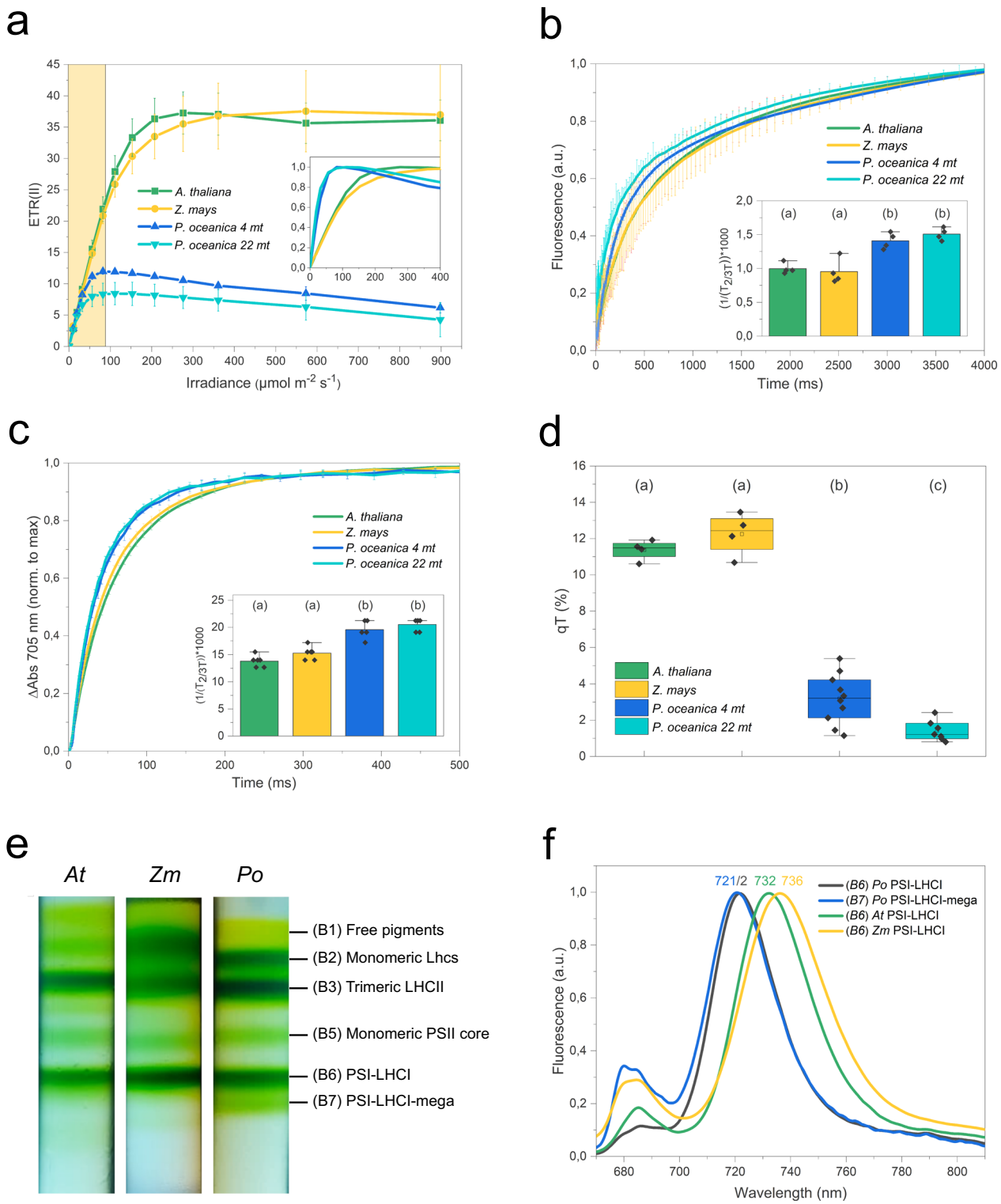

(Supplementary Fig. 9a, b). B7 revealed the structure of PSI-LHCI-mega complex (Fig. 2d, e), reconstructed at 3.31 Å (Supplementary Fig. 6d–f). Cryo-EM maps showed clear densities corresponding to a trimeric LHCII and an additional LHCI dimer bound near the PsaH-PsaI side of the PSI core, extending the canonical PSI-LHCI architecture. Furthermore, the trimeric LHCII was positioned to interact with the extra LHCI dimer on one side and with the PsaO and PsaK subunits on the other (Fig. 2d). Notably, PsaO was only detected in the PSI-LHCI-mega. Despite slightly lower local resolution (Supplementary Fig. 6f), the density maps were clear enough to unambiguously assign the trimeric LHCII and additional LHCI as an Lhca1-4 heterodimer (Supplementary Figs. 10–12). The final PSI-LHCI-mega model comprises the PSI core surrounded by three LHCI heterodimers and one LHCII heterotrimer, containing 22 protein chains, 289 pigments (194 Chl *a*, 36 Chl *b*, 33 β-carotenes, and 26 xanthophylls), 3 Fe_4S_4 clusters, and 26 lipid molecules (Fig. 2f, Supplementary Fig. 8b and Supplementary Table 2).

The LHCII trimer in the PSI-LHCI-mega contained Lhcb1 and Lhcb2 subunits (Supplementary Fig. 3f), consistent with "mobile" LHCII trimers of land plants[33,34]. Based on the similarity with the PSI-LHCI-LHCII structures of *Z. mays*[31], *A. thaliana*[32], and the well-defined density maps

Fig. 1 | Photosynthetic performance and supercomplex organization in *P. oceanica*. **a** Relative electron transport rate of PSII (ETR-II) dependence on irradiance in intact leaves of *P. oceanica* (4–22 mt depth), *A. thaliana*, and *Z. mays*. Data are presented as mean values ± sd ($n = 3$, biological replicates). Inset: mean ETR-II normalized to its maximum value. **b** Functional PSII cross-section determined from Chl fluorescence induction kinetics in thylakoid membranes, in the presence of DCMU. Inset: functional cross-section expressed as the reciprocal of the time to reach 2/3 of maximum fluorescence (ms^{-1}). Data are presented as mean values ± sd ($n = 4$, biological replicates). **c** Functional PSI cross-section assessed by P700 oxidation kinetics at 705 nm in thylakoid membranes, in the presence of methyl viologen and ascorbate. Inset: functional cross-section expressed as the time to reach 2/3 maximum oxidation level (ms^{-1}). Data are presented as mean values ± sd ($n = 6$ for *A. thaliana* and *Z. mays*, and *P. oceanica* 22 mt; $n = 5$ for *P. oceanica* 4 mt, all of which are biological replicates). **d** Extent of PSII fluorescence quenching during State 1-State 2 transitions (Supplementary Fig. 2d), expressed as qT (%). Box plots showed the 25th–75th percentiles, the median (center line), whiskers indicating the minimum and maximum values, and the empty square representing the mean of biological replicates ($n = 4$ for *A. thaliana* and *Z. mays*, $n = 10$ for *P. oceanica* 4 mt, and $n = 7$ for *P. oceanica* 22 mt). In (**b**–**d**), statistical differences were determined using a one-way ANOVA followed by Tukey's test and are indicated by lower-case letters (*P*-values < 0.005 for panels **b**, **c**; *P*-values < 0.05 for panel **d**. Black rhombi represent individual biological replicates. **e** Separation of pigment-protein complexes by sucrose density gradient ultracentrifugation from *A. thaliana* (*At*), *Z. mays* (*Zm*), and *P. oceanica* (*Po*) at 22 mt depth thylakoids solubilized with final 1% β-DDM (v/w). **f** Low-temperature (77 K) fluorescence emission spectra (normalized to the maximum $\lambda_{emission}$) of PSI-LHCI complexes from B6 and B7. $\lambda_{excitation} \leq 448$ nm. Source data are provided as a Source Data file.

of the N-terminal domain, the Lhcb monomer extending towards the PsaL-PsaO subunits was assigned as Lhcb2, with the remaining two chains modeled as Lhcb1 proteins, based on immunoblots of Supplementary Fig. 3f. This arrangement resembled that observed in PSI-LHCI-LHCII (ST2) isolated from land plants[31,32] and, in part, to the PSI megacomplex isolated from the moss *Physcomitrella patens*[35] (Supplementary Fig. 13).

A distinct feature of this LHCII trimer is a phosphorylated Thr located at the N-terminus of Lhcb2, mediating interactions with core subunits. This residue is part of a highly conserved Arg-Arg-pThr motif (R37-R38-pT39 in *P. oceanica*, Supplementary Fig. 14a), in which the phosphate group interacts with PsaL via a salt bridge with the side chain of R170 and a hydrogen bond with the hydroxyl group of T168, while the guanidinium nitrogen of R37 forms a hydrogen bond with the hydroxyl group of G78 in PsaH. Additional polar contacts occur between R38 and the side chains of N62 and E71 of PsaL, as well as between its carbonyl oxygen and the nitrogen of the R52 side chain of PsaO (Fig. 3a, Supplementary Fig. 14b). The interaction is further stabilized by hydrophobic contacts between the helix spanning residues 59–75 of PsaO and the second transmembrane helix of a Lhcb1 protomer (Fig. 3b, Supplementary Fig. 14b), as well as by a hydrogen bond connecting N60 of PsaO with the aldehyde oxygen of Chl *b*601 of $Lhcb2_Y$, consistent with[31]. Although pigment analysis showed a lower Chl a/*b* ratio in *Po*LHCII (Supplementary Fig. 3a, b) relative to land plants, the local resolution of the Cryo-EM maps in this region is insufficient to distinguish between Chl *a* and *b*. Therefore, the pigments were modeled based on the structures of the land plants[31,32]. Chl-binding sites analysis revealed a conserved Phe-to-Tyr mutation near Chl 603 in *P. oceanica*, present in all three *Po*LHCII isoforms, which creates a more polar environment and could enable a hydrogen bond between the formyl group of Chl *b* and the hydroxyl group of Tyr side chain (Supplementary Fig. 14c, d), suggesting a location for the additional Chl *b*-binding site.

A distinctive feature of the PSI-LHCI-mega complex is the presence of an additional Lhca1-Lhca4 (hereafter referred to as $Lhca1_5$-$Lhca4_6$; Fig. 2d–f). This dimer is positioned in a region of the supercomplex reminiscent of that occupied by the Lhca9-Lhca2 dimer in *Chlamydomonas reinhardtii* (*Cr*) PSI[14] (Supplementary Fig. 13), but its interaction with the core subunits is markedly different. The main contacts are mediated by $Lhca4_6$ with the PsaH and PsaI chains (Fig. 3c): three negatively charged residues in $Lhca4_6$ (E85, D86, and E88), located in the loop preceding its first transmembrane helix, face two positively charged residues (K102 and K108) on the surface of PsaH. Additional stabilization arises from hydrogen bonding between the NZ nitrogen of K91 in PsaH and the carbonyl oxygen of P71 in $Lhca1_5$, as well as hydrophobic interactions between L88 of PsaH and L73 and L75 of $Lhca1_5$. Furthermore, a short antiparallel β-sheet formed by the N-terminal residues of PsaI (D3 and L4) and the C-terminal residues of $Lhca4_6$ (T250-S252) contributes to further stabilizing the $Lhca1_5$–$Lhca4_6$ dimer binding to the PSI core (Fig. 3c).

The $Lhca1_5$-$Lhca4_6$ dimer also interacts with the LHCII trimer: the second transmembrane helix of $Lhca1_5$ (T139-P141) contacts the loop between the first and second helices of $Lhcb2_Y$ (P148-V151). These interactions likely stabilize the LHCII-PSI core interaction, allowing the higher stability of the PSI-LHCI-mega compared with other PSI-LHCII supercomplexes[31,32], even under β-DDM extraction. In *A. thaliana*, a more compact PSI-LHCI conformation has been reported during the ST1-2, involving shifts in the Cα positions of several chains, particularly the four LHCI subunits[32]. In contrast, superposition of the *Po*PSI-LHCI structure with that of the PSI-LHCI-mega revealed a root mean square deviation of only 0.38 Å, indicating minimal structural changes upon binding of the additional LHC subunits (Supplementary Fig. 15). Notably, the long stromal loop of PsaK (residues 71-101), which is disordered in canonical PSI-LHCI, adopts a more defined conformation in the presence of PsaO and the LHCII trimer in PSI-LHCI-mega.

Excitation energy transfer network of PSI-LHCI-mega

To identify EET pathways within the PSI-LHCI-mega, we modeled the interactions between Chl molecules using site-energy-scaled Förster Resonance Energy Transfer (FRET) (see Supplementary Methods). We identified 230 Chl molecules in the PSI-LHCI-mega (Fig. 2f), whose relative distance and orientations were used to derive the potential EET pathways between different LHCs, and EET to the core subunits via the LHCII trimer and extra $Lhca1_5$-$Lhca4_6$ dimer, as well as via the LHCI belt (Supplementary Fig. 16a-b). The overall preferential EET routes to the PSI core in PSI-LHCI-mega are shown in (Fig. 4, Supplementary Tables 3, 4). Although most of the main EETs are similar to those described for other PSI-LHCI-LHCII[14,31,32,35], the presence of the $Lhca1_5$-$Lhca4_6$ dimer, which interacts with both the core subunits and the trimeric LHCII, led to the identification of additional EET pathways. Our model suggests that the energy transfer paths from the $Lhca1_5$-$Lhca4_6$ dimer involve the PsaH and PsaL, following the route: $Lhca4_6 \rightarrow Lhca1_5 \rightarrow$ PsaH → PsaL → PsaA, with Chl *a*602/5 and *b*607/5 being the best candidates to funnel excitation energy towards Chl *a*209/H. Excitation may then reach PsaL via Chl *a*306, and then *a*843/A through Chl *a*307/L or *a*308/L. Notably, Chl *b*607/5 and *a*606/5 may receive part of the excitation energy from the LHCII trimer through Chl *b*605/Y and deliver it to the core. Alternatively, excitation from Chls of $Lhcb1_X$ and $Lhcb1_Z$ can reach Chls *b*601/Y and *a*614/Y of $Lhcb2_Y$, from where it is delivered to Chls *a*203-*a*204/O and eventually reaches PsaA through Chls *a*857-*a*823-*a*824-*a*825, consistent with pathways observed in the *Z. mays*[31].

EETs within and from the LHCI belt to the PSI-core are similar to those reported for canonical PSI-LHCI[28,30]. Lhca1 mainly transfers energy to the PsaB side via Chls *a*603-*a*606-*b*607-*a*609, which lie close to Chls *a*820-*a*821-*a*840 of PsaB, and *a*223/G. Instead, energy from Lhca4 reaches Lhca1 via Chl *b*607/4 → *a*617/1 and is subsequently delivered to *a*317/F. Lhca2 contributes via multiple paths (e.g., *b*606/2 → *a*601/4 or *b*616/2 → *a*601/4), or transfers directly to

https://doi.org/10.1038/s41467-026-75200-8

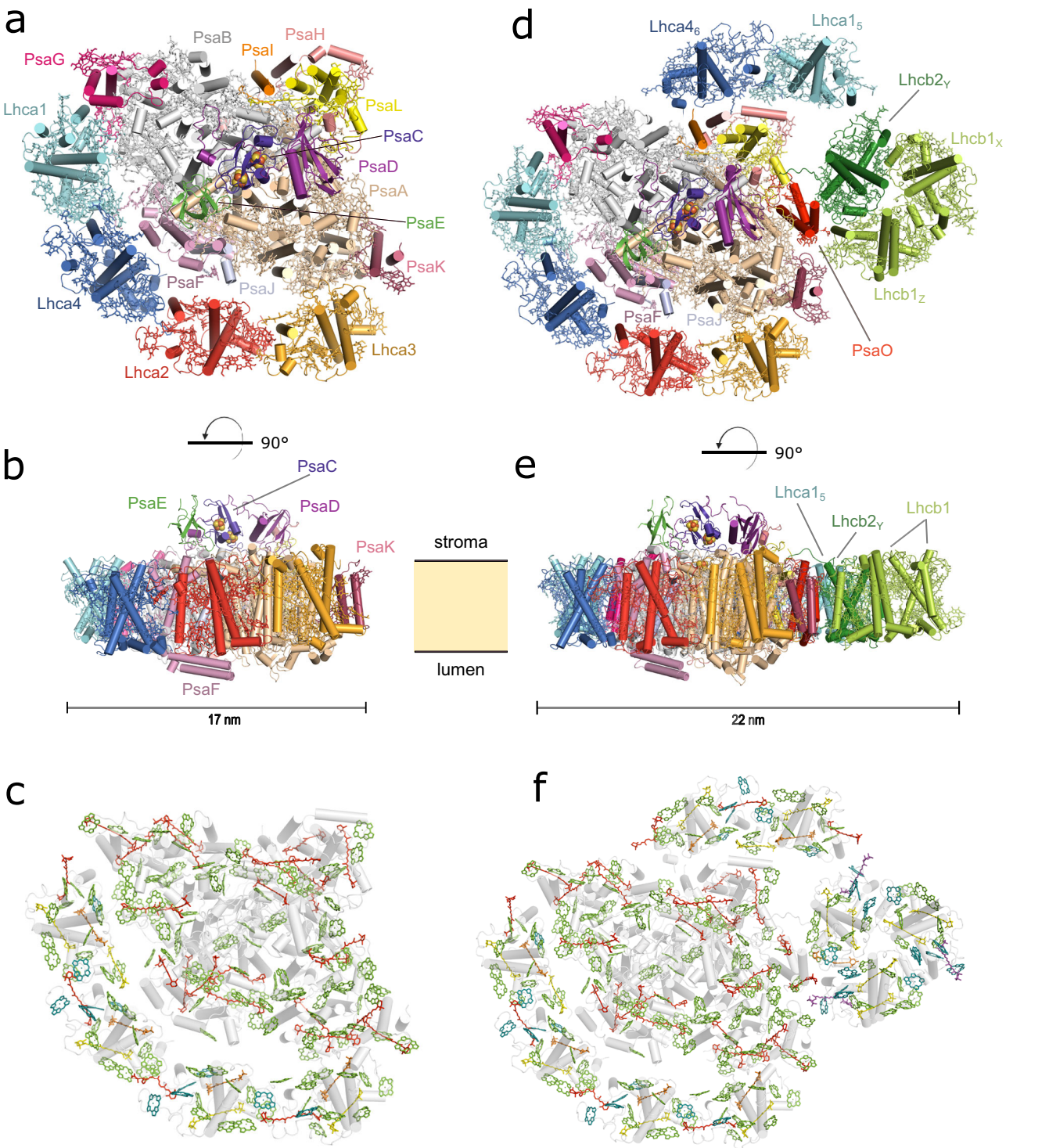

Fig. 2 | Overall structure of *P. oceanica* PSI-LHCI supercomplexes. a–c PSI-LHCI complex. **d–f** PSI-LHCI-mega complex. **a**, **d** Stromal views. **b**, **e** Side views (membrane orientation indicated). **c**, **f** Pigment arrangement in the same orientation as in (**a**, **d**). Pigments and lipids are shown as stick models, and Fe_4S_4 clusters are depicted as spheres. Subunits are colored as follows: Lhca1, light blue; Lhca2, red; Lhca3, light orange; Lhca4, blue; PsaA, wheat; PsaB, gray; PsaC, purple blue; PsaD, purple; PsaE, green; PsaF, pink; PsaG, hot pink; PsaH, salmon; PsaI, orange; PsaJ, bluwhite; PsaK, raspberry; PsaL, yellow; PsaO, dark red; Lhcb2, forest; Lhcb1 (x and z), lemon. Pigments: Chl *a*, green forest; Chl *b*, teal; β-carotene, red; lutein, yellow; violaxanthin, orange; neoxanthin, magenta.

PsaJ through *b*607/2 → *a*102/J. At the same time, Lhca2 is also coupled with Lhca3, mainly through the connections *b*601/2 → *a*615/3 and *a*614/2 → *a*606/3. From Lhca3, excitation energy reaches Chls *a*811-*a*813 of PsaA through Chls *a*603/3-*a*602/3, or *a*202/K through *a*613/3 (Fig. 4).

Time-domain measurement of ultrafast excitation energy transfer

To experimentally track the time-domain ultrafast EET processes in *P. oceanica* complexes, we used 2DES (see Supplementary Methods). This technique simultaneously maximizes temporal and spectral

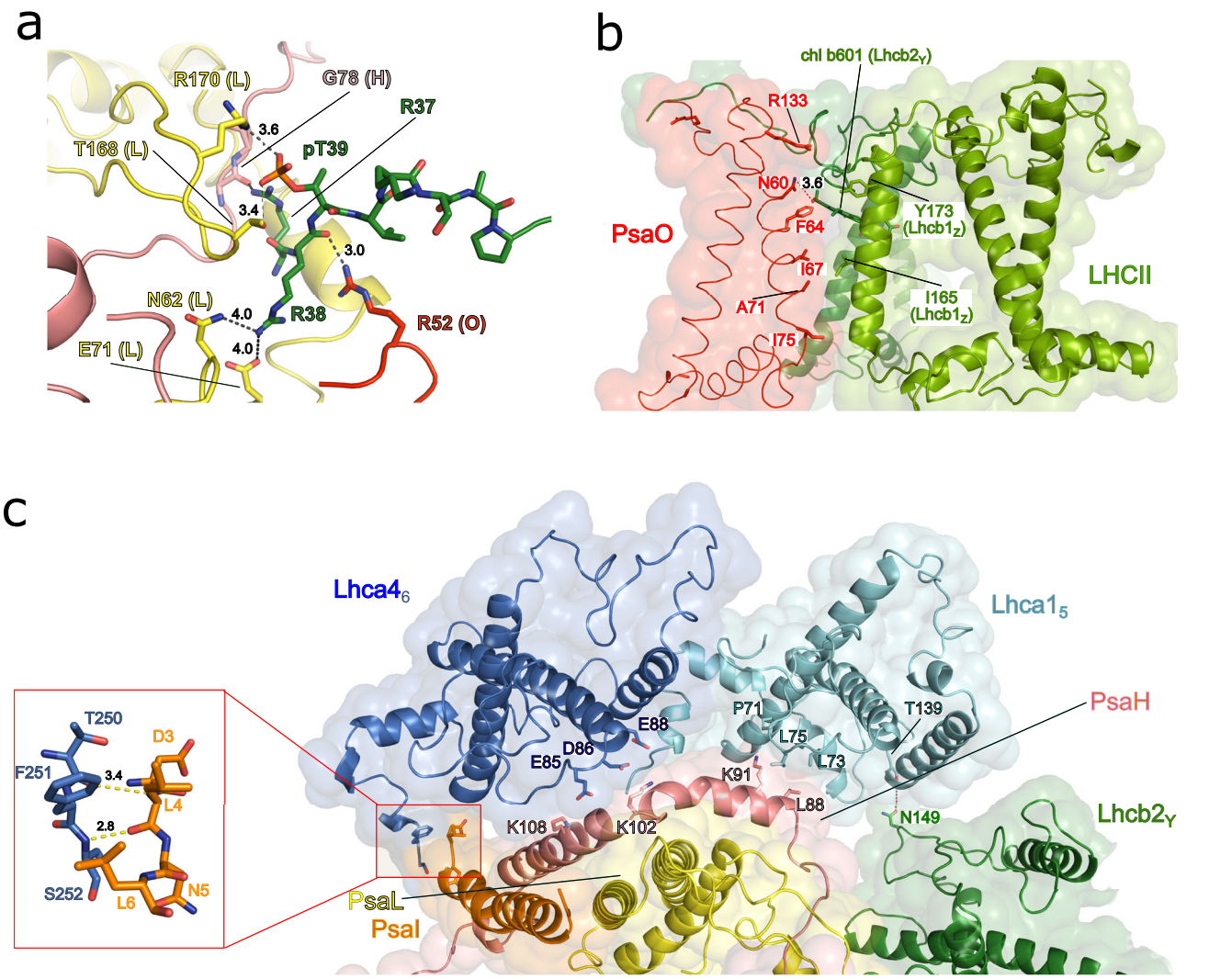

Fig. 3 | Interactions between the LHCII trimer and the Lhca1$_5$-Lhca4$_6$ dimer with the PSI-core in PSI-LHCI-mega. a Main interactions (dashed lines) between side chains of the N-terminal phosphorylated motif (R37-R38-pT39) of Lhcb2$_Y$ (green) and the core subunits PsaH (pink), PsaL (yellow), and PsaO (red). **b** Transmembrane interface between PsaO (red) and the LHCII trimer subunits. The protein main chain is shown as a ribbon (PsaO) or cartoon (LHCII) model, with solvent-accessible surfaces displayed in transparency. Side chains of the contact surface residues and Chl *b*601 of Lhcb2$_Y$ are shown as sticks. **c** Interactions of the Lhca1$_5$-Lhca4$_6$ dimer (cyan-blue) with the core subunits PsaH (pink), PsaI (orange), and Lhcb2$_Y$ (dark green). Proteins are drawn as cartoon models with solvent-accessible surfaces in transparency. Side chains of relevant residues are shown as sticks. The small β-structure stretch between the N-terminus of PsaI and the C-terminus of Lhca4$_6$ is highlighted in the red box. Small black numbers in (**a**–**c**) indicate the distances in Å.

resolution[36] by recording 2D maps that correlate the wavelengths of excitation and detection as a function of the population time t_2. Thus, 2DES enables direct visualization of EET processes via the t_2 dependence of the cross-peaks' amplitudes[37]. We performed 2DES experiments on *Po*PSI-LHCI and PSI-LHCI-mega (Fig. 5, Supplementary Figs. 17, 18), and compared the results to those previously obtained for the land plant PSI-LHCI[38]. The 2DES map of the *Po*PSI-LHCI at $t_2 = 100$ fs (Fig. 5a) showed a dominant diagonal peak near 680 nm, which is assigned to the ground-state bleaching of the bulk Chl band. Cross peaks also appear upon excitation between 600 nm and 640 nm (Chl *b*) and detection in the 680 nm band. These are consistent with rapid EET from Chls *b* into the bulk Chl *a* manifold. Notably, there are no significant features above 700 nm, which is consistent with the absence of low-energy Chl forms. Figure 5b showed the cross-peak dynamics at specific excitation and detection wavelengths (excitation at 630 nm, detection at 670, 680, and 696 nm). The traces at the 670- and 680-nm detection wavelengths exhibit a multi-exponential decay. In contrast, the ~696 nm detection wavelength (which corresponds to the RC/P700 spectral region) exhibits an ultrafast rise followed by a slower decay. This is consistent with the rapid population of RC-associated states. A global analysis of the full 2DES dataset using a sum of exponentials identified four components: $\tau_1 = 50$ fs, $\tau_2 = 960$ fs, $\tau_3 = 6.3$ ps, and a non-decaying contribution within the 100 ps experimental temporal window (Supplementary Fig. 19a). We assigned τ_1 to the relaxation of higher-energy Chl states into the bulk Chl ~680 nm band and to energy redistribution within that band. We assigned τ_2 to ultrafast EET from the bulk Chl manifold toward the RC (population growth in the P700-associated spectral region). Finally, we assigned τ_3 to RC trapping/charge separation, which is consistent with the formation of the oxidized donor state ($P700^+$). The non-decaying component reflects long-lived RC- and/or Chl-associated signals that persist beyond the measurement time window. Figure 5c shows the Jablonski diagram for the PSI-LHCI, summarizing all EET pathways and their associated time constants. The same measurements and analyses performed on the PSI-LHCI-mega (Fig. 5d–f) reveal closely related spectral signatures and dynamic processes. The 2DES map at $t_2 = 100$ fs

https://doi.org/10.1038/s41467-026-75200-8

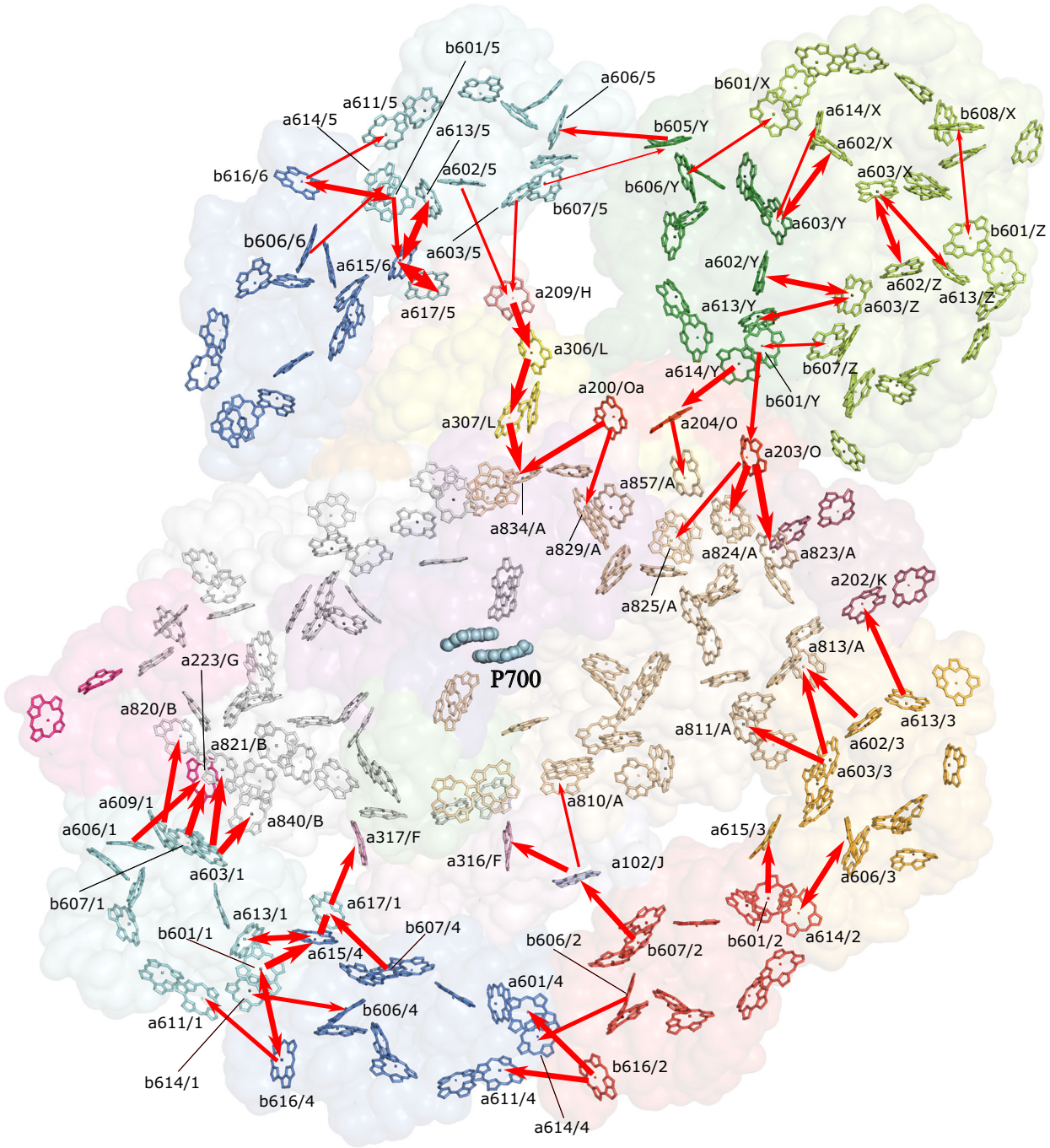

Fig. 4 | Excitation Energy Transfer (EET) pathways in PSI-LHCI-mega. Red arrows indicate the strongest plausible Chl-Chl EET pathways modeled by Förster Resonance Energy Transfer. Protein subunits and their pigments are colored according to the color code in Fig. 2. Arrow thickness is proportional to the calculated k_{EET} magnitude. The corresponding k_{EET} values are reported in Supplementary Tables 3, 4 and Supplementary Data 1.

(Fig. 5d) showed a broader and more intense cross-peak at a detection wavelength of ~680 nm, which is consistent with an increased effective contribution of Chl *b*. The dynamics (Fig. 5e) are qualitatively similar to those observed for *Po*PSI-LHCI. A global fit of the 2DES maps (Supplementary Fig. 19b) again requires three time constants plus a non-decaying term: $\tau_1 = 70$ fs, $\tau_2 = 730$ fs, and $\tau_3 = 12$ ps (Fig. 5f). While τ_1 and τ_2 are comparable to those of *Po*PSI-LHCI, the trapping component τ_3, is approximately twice as slow in the PSI-LHCI-mega, which is consistent with a longer effective energy migration pathway before trapping in RC (P700 oxidation).

A comparison with the land plant PSI-LHCI[38] (Fig. 5g–i) reveals a significant qualitative distinction. The $t_2 = 100$ fs map exhibits a clear diagonal feature near ~710 nm (Fig. 5g), suggesting a significant contribution from low-energy Chl forms that were absent in *P. oceanica*. Low-energy Chl forms' involvement in the light-harvesting process is reinforced by cross-peak dynamics (Fig. 5h). A build-up at the ~710 nm detection wavelength indicates energy flow into low-energy Chl forms. Meanwhile, the dynamics at the 670/680/696 nm detection wavelengths are comparable to those of the *P. oceanica* complexes. Global analysis of land plant PSI-LHCI requires five time constants (Fig. 5i):

https://doi.org/10.1038/s41467-026-75200-8

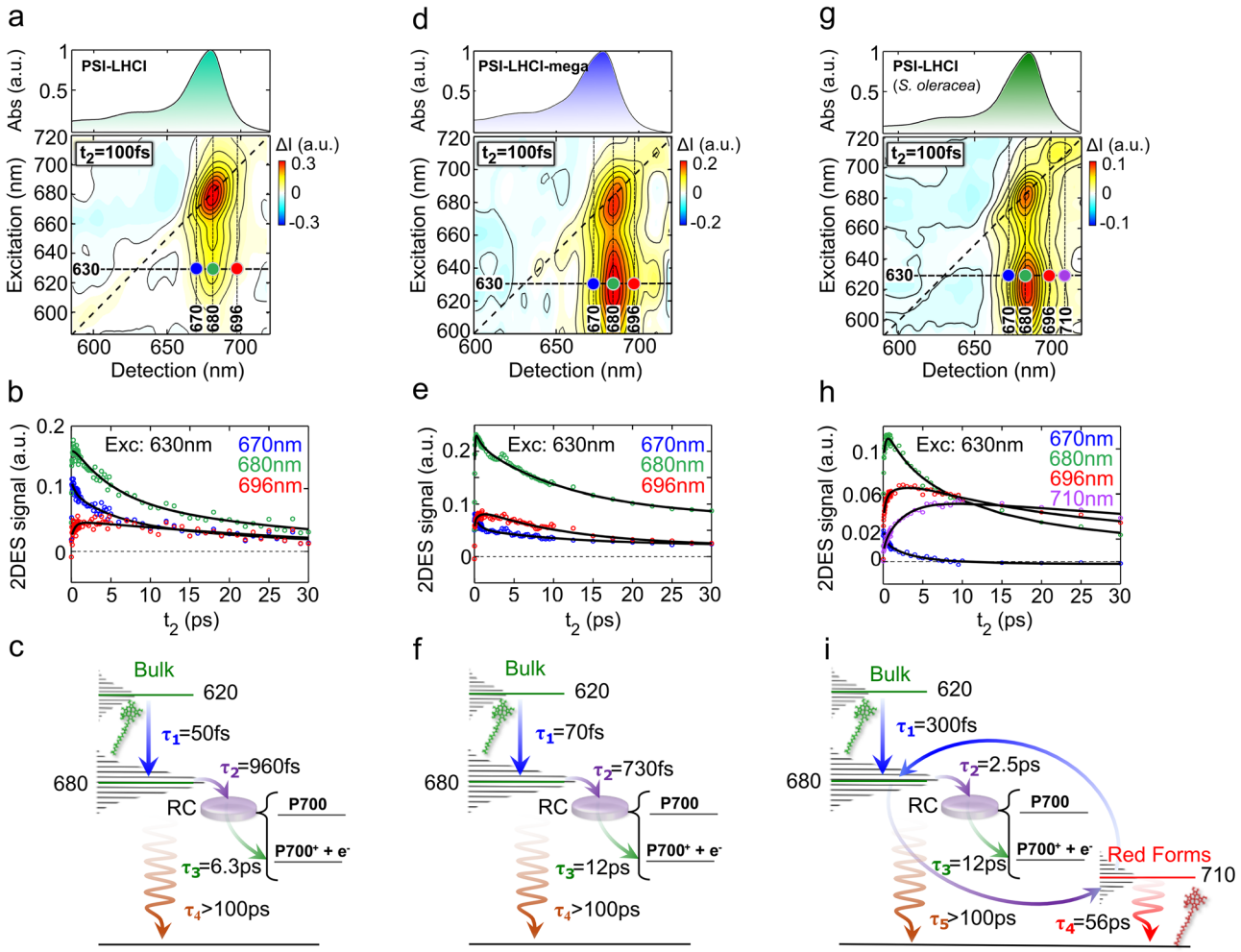

Fig. 5 | Detection of ultrafast Excitation Energy Transfer (EET) in *P. oceanica* PSI-LHCI and PSI-LHCI mega, compared to land plant PSI-LHCI. a, d–g 2DES maps at $t_2 = 100$ fs of PSI-LHCI (**a**), PSI-LHCI-mega (**d**), and land plant PSI-LHCI isolated from *S. oleracea*[38] (**g**), together with the corresponding absorption spectra (upper panel). **b, e–h** Dynamics at selected cross peaks corresponding to excitation at 630 nm and detection at: 670 nm (blue), 680 nm (green) and 696 nm (red) for PSI-LHCI (**b**) and PSI-LHCI-mega (**e**), and at 670 nm (blue), 680 nm (green), 696 nm (red) and 710 nm (violet) for *S. oleracea* PSI-LHCI (**h**); **c**, **f–i** Jablonski diagrams, with time constants obtained from global fits of the 2DES measurements, for PSI-LHCI (**c**), PSI-LHCI-mega (**f**), and *S. oleracea* PSI-LHCI (**i**), drawn according to refs. 38,58. Source data are provided as a Source Data file.

$\tau_1 = 300$ fs, $\tau_2 = 2.5$ ps, $\tau_3 = 12$ ps, τ_4=56 ps, plus a non-decaying component. τ_1 describes the redistribution among higher-energy and bulk Chl states, including low-energy Chl forms-related equilibration. τ_2 reflects the slower bulk Chl-to-RC energy transfer compared to *P. oceanica*. τ_3 indicates a trapping/charge-separation timescale similar to that of PSI-LHCI-mega, but approximately twice as slow as in *Po*PSI-LHCI. Overall, these comparisons are consistent with models in which the presence (or absence) of low-energy Chl forms reshapes the energy landscape and can measurably alter the effective EET kinetics and trapping at the RC/P700[38–40]. Meanwhile, *P. oceanica* exhibited faster EET kinetics, while also maintaining efficient trapping even in its larger antenna assemblies. The wavelength-dependent mean decay lifetime maps (τ_m) derived from global analysis of 2DES data (Supplementary Fig. 20a, b) support this interpretation. In particular, the weaker dependence of τ_m on the detection wavelength observed for *P. oceanica* supercomplexes compared to land plant PSI-LHCI (Supplementary Fig. 20c–e) reflects the absence of low-energy Chl forms.

Structural determinants for suppression/repletion of low-energy Chl forms

Low-energy Chl forms, originating from the Chls *a*603-*a*609 cluster in Lhca3 and Lhca4, are responsible for absorption beyond 700 nm in land plant PSI-LHCI and are detected in the 77 K fluorescence emission spectra[26,41,42]. Figure 1f showed that *Po*PSI-LHCI, irrespective of size, displayed a blue-shifted fluorescence emission compared to the >730 nm emission typical of land plants, while 2DES maps (Fig. 5) revealed no significant features above 700 nm, indicating loss of low-energy forms in LHCI[21,26]. This loss correlates with faster EET and shorter trapping times toward the RC/P700 compared to the >730 nm-emitting PSI-LHCI of land plants[38,40]. Faster trapping might be advantageous under dim light; thus, we examined the structural determinants controlling chromophore organization responsible for low-energy Chl forms in *P. oceanica*.

An Asn residue serving as a ligand for Chl *a*603 in Lhca3 and Lhca4, instead of His in low-energy form-depleted LHCs, was previously identified as crucial for forming low-energy forms[25,26]. The Asn ligand allows closer spacing between *a*603 and *a*609, enabling a stronger coupling between the exciton and charge transfer[25,26,42]. Indeed, blue-shifted green algae PSI features His as Chl *a*603 ligand, while Asn-to-His mutations in land plants abolished low-energy forms in both recombinant and native systems[25,26,43,44]. Surprisingly, the fluorescence blue-shift observed in *Po*PSI-LHCIs (Fig. 1f) occurs despite Asn retention as the Chl *a*603 ligand in both Lhca3-4 (Supplementary Fig. 21). The well-resolved density maps around the *a*603-*a*609 cluster

https://doi.org/10.1038/s41467-026-75200-8

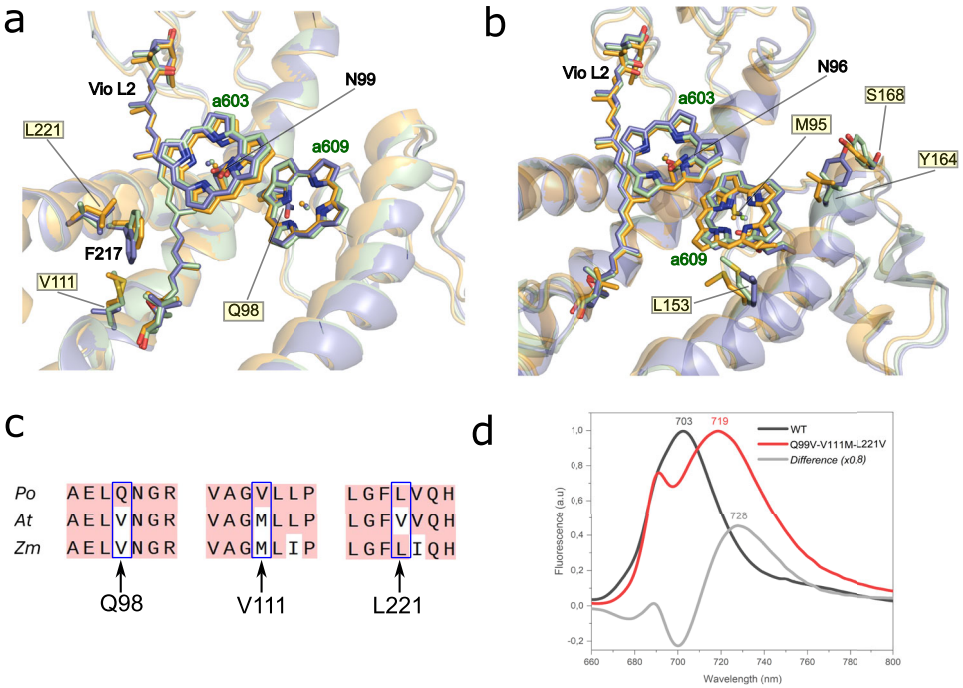

Fig. 6 | The local protein environment and pigment organization of the low-energy Chls cluster of *P. oceanica* Lhca3 and Lhca4. Structural comparison of Lhca4 (**a**) and Lhca3 (**b**) from *P. oceanica* (lavender), *Z. mays* (orange), and *A. thaliana* (green). The superimposition was obtained by aligning the Cα position of the different proteins. Chls *a*603-*a*609, violaxanthin (Vio) L2, and relevant side chains are shown as sticks. **c** Sequence alignments of three regions of Lhca4 around the low-energy Chls cluster. The mutations in *P. oceanica* (labeled with a yellow background in (**a**, **b**) are indicated with arrows. **d** 77 K fluorescence emission spectra (normalized to maximum $\lambda_{emission}$) of recombinant *Po*Lhca4 WT (black line) and Q99V-V111M-L221V mutant (red line), with the difference spectrum (mutant minus WT) in gray. $\lambda_{excitation} \leq 448$nm. Source data are provided as a Source Data file.

in *Po*PSI-LHCI (Supplementary Fig. 22a, b) enabled accurate modeling of the positions and orientations of the two chlorin rings (Supplementary Fig. 22c, d). Superposition of Lhca4 structures from *P. oceanica*, *Z. mays*, and *A. thaliana* (Fig. 6a) revealed conserved Chl *a*609 positioning, while Chl *a*603 was displaced and located farthest from Chl *a*609 in *P. oceanica*. Sequence comparison identified three mutations surrounding the cluster: Q98, V111, and L221 (Fig. 6c), potentially influencing Chl *a*603 location in Lhca4. The smaller side chain of V111 versus Met allows the F217 aromatic ring to shift away from the Chl *a*603 chlorine ring. In *Z. mays* and *A. thaliana*, the bulkier Met sidechain forces F217 into a different rotameric conformation, pushing the chlorine ring closer to Chl *a*609. The smaller L221 side chain versus Val in *A. thaliana* may also favor this displacement. Additionally, the Val-for-Gln substitution at position 98 likely induces an outward shift of Cα of the coordinating residue (N99). As a result, the distance between E-ring centers of the Chls *a*603-*a*609 changes from 4 Å in *Z. mays* to 4.5 Å in *P. oceanica* (Supplementary Fig. 23a, b). This increased spacing reduces orbital overlap, weakening the coupling responsible for low-energy absorption (Supplementary Fig. 24). In Lhca3, a distinct pattern emerged: Chl *a*603 retained its position across *P. oceanica*, *Z. mays*, and *A. thaliana* structures (Fig. 6b), while Chl *a*609 was further displaced in *P. oceanica*, likely due to a shift in the second transmembrane helix housing the coordinating Glu (E160). Thus, despite arising from different protein domain changes, both Lhca3 and Lhca4 lose low-energy forms through increased *a*603-*a*609 separation, leading to reduced E-ring overlap compared with *Z. mays* and *A. thaliana* (Supplementary Figs. 23, 24).

To confirm the role of these mutations, we cloned and expressed in *E. coli* a His-tagged *Po*Lhca4 WT and a triple mutant Q99V-V111M-L221V (Supplementary Fig. 25a–c), restoring the land plant sequence within the low-energy cluster. The recombinant mutant exhibited a red-shifted 77 K fluorescence peak by ~16 nm (703 → 719 nm, Fig. 6d), along with increased low-energy absorption (> 700 nm), supported by circular dichroism spectra (Supplementary Fig. 25d, e). The mutant also showed an increased average fluorescence lifetime (Supplementary Fig. 25f, g)[43]. Emission difference spectra revealed a strong 728 nm contribution (Fig. 6d), indicating full recovery of the low-energy forms relative to *A. thaliana* rLhca4[25], and confirming that Q99V-V111M-L221V are key residues shaping the conformation of the low-energy Chl cluster.

Discussion

P. oceanica meadows are highly productive[3,4] with net productivity up to 12 g DW/m²/day[3], comparable to 10–20 g DW/m²/day during peak rice growth, despite far lower irradiance. This implies higher light-use efficiency even though ETR is lower (Fig. 1a). Photosynthesis in land plants is limited by light, temperature, and CO_2, dissipating ≥50% of absorbed energy. *P. oceanica* is not limited by CO_2[45] nor drought, while temperature is far less variable, allowing minimal light stress, low NPQ (Supplementary Fig. 2a), and perennial growth; starch reserves support biomass accumulation under less favorable conditions[3]. Depth and shading by epiphytes and canopy reduce photon fluence, making the differential ETR rate (Fig. 1a, inset) relevant for growth rate. Adaptation to the marine light environment involves both intensity- and spectrum-dependent mechanisms. Selective light absorption and scattering underwater cause rapid attenuation of red and far-red radiation, yielding blue-green irradiation already at 4 m depth and a progressive decrease in photon fluence (Supplementary Fig. 1c). The physiological response includes enhancement of both PSI and PSII functional cross-section, increasingly with depths, compared to those of land plants (Fig. 1b, c). Pigment-protein analysis revealed the presence of a PSI with an expanded antenna system, renamed PSI-LHCI-mega (B7, Fig. 1e), whose abundance corresponded to a PSI-LHCI-mega/PSI-LHCI ratio of ~0.3, based on densitometric analysis (Supplementary Fig. 2c), with limited depth-dependent variation.

Acclimation differences between photosystems are likely compensated by changes in the PSI/PSII ratio[21]. Spectral adaptation also involves increased Chl *b* and xanthophyll content in trimeric LHCII (Supplementary Fig. 3b, g), enhancing blue light absorption[21]. Remarkably, LHCI-associated low-energy Chl forms typical of land plants are missing (Fig. 1f). Although low-energy forms evolved over ~500 million years during land plant evolution, they were secondarily lost less than ~70 million years ago when seagrass lineages returned to the sea, a pattern also reported for *Cymodoceaceae* and *Zosteraceae*[21,26]. Because low-energy forms confer a selective advantage under far-red-enriched canopies, their evolutionary loss in seagrass is consistent with infrared radiation extinction by water[26]. Low-energy Chl forms can effectively limit EET kinetics and exciton trapping to the RC/P700[38,39]. In contrast, *Po*PSI-LHCI exhibits faster and more efficient EET kinetics and trapping (Fig. 5a–c). Furthermore, PSI-LHCI-mega, which contains five additional LHC subunits, PsaO, and 75 more Chls than the canonical PSI-LHCI, maintains highly efficient EET, displaying ~four-fold faster kinetics than the land plant PSI-LHCI, while retaining comparable exciton trapping time at RC/P700 (Fig. 5d–i). This indicates well-interconnected LHCs despite a greater distance from the core and is consistent with a scenario in which the antenna expansion is compensated by the loss of low-energy Chl forms. Overall, this reflects a finely tuned balance or potential trade-off between antenna size and quantum efficiency, enabling an increased absorption cross-section without losing efficiency. Fast exciton trapping is likely advantageous in *P. oceanica* meadows, where light availability, already attenuated by the water column, is further reduced by canopy self-shading and dense epiphytic colonization of leaves[8], making an efficient exciton trapping within expanded antenna systems a key adaptive advantage. During green lineage evolution, LHCI-low-energy forms were associated with the His → Asn substitution at the Chl *a*603 ligand in Lhca3 and Lhca4 antennas[25]. Since His side chain is bulkier than Asn, Asn-to-His mutation in *A. thaliana* increases the distance between Chl *a*603-*a*609, disrupting the mixing between excitonic and charge-transfer states[25,26]. This results in loss of low-energy forms, implying that inter-porphyrin distance and orbital overlap determine their genesis[26,42]. Our structural analysis showed that sequence changes leading to their loss in *P. oceanica* retained Asn as the Chl *a*603 ligand, preserving the vertical separation between the porphyrin planes (Fig. 6). Instead, in *Po*Lhca4, mutations are located around the plane of Chl *a*603. Although the residue Phe 217 is conserved, its aromatic ring orientation defines the pocket width accommodating Chl *a*603, thereby allowing it to slide horizontally further away from Chl *a*609 (Fig. 6a). This orientation is modulated by Val replacing bulkier Met at position 111 and by Val at 221. Additionally, replacing Val98 with Gln induces a slight displacement of Asn99, which coordinates Chl *a*603. Mutating these three residues to their land plant orthologs restored the low-energy forms in recombinant *Po*Lhca4 (Fig. 6d), confirming that steric interference drives the repositioning of Chl *a*603 closer to Chl *a*609. In *Po*Lhca3, Chl *a*603 position is maintained, but Chl *a*609 is shifted away by a bend in transmembrane helix C, housing its ligand Glu 160. Consequently, the E-ring overlap of Chl *a*603-*a*609 is reduced (Fig. 6b, Supplementary Fig. 23d). Lhca3-4 of land plants, which have low-energy Chl forms, display larger E-ring overlap than *P. oceanica* (Supplementary Figs. 23, 24). Thus, E-ring overlap is a key factor for establishing charge-transfer states between Chl *a*603 and Chl *a*609[26,42], whenever the chlorin ring planes are <4.5 Å apart (Supplementary Fig. 24). The distinct mutations linked to the loss of low-energy Chl forms in *P. oceanica* are suppressive mutations that revert to an evolutionary ancestral state and reproduce the structure of an aquatic organism lacking LHCI-low-energy forms. These findings represent an important step toward the synthetic biology of light-harvesting systems, which could be engineered to fine-tune their absorption properties and optimize photon capture under far-red-enriched dense canopies[9].

We further report the high-resolution structure of PSI-LHCI-mega, which is unique among PSI supercomplexes reported in higher plants so far (Supplementary Fig. 13). The most similar structures are those of PSI-LHCI-LHCII in *Z. mays* and *A. thaliana*[31,32], which, however, both lack the Lhca1$_5$-Lhca4$_6$ dimeric complex bound to PsaH and PsaI. A similar LHCI dimer has been found in *C. reinhardtii* PSI-LHCI, but it interacts with different core subunits, namely PsaG and PsaB. The docking position enables Lhca1$_5$-Lhca4$_6$ to interact with the trimeric phosphorylated LHCII, resulting in a more stable complex than the fast-reversible assemblies observed upon ST (Supplementary Fig. 13). Stabilizing contact points between Lhca1$_5$-Lhca4$_6$ include the C-terminus of Lhca4$_6$, which forms a short β-sheet with the N-terminus of PsaI. This interaction is favored by a Leu substituting for a bulky Phe at the corresponding position of *Z. mays* and *A. thaliana* Lhca4. This side-chain position did not interact with neighboring subunits in Lhca4, allowing for mutation without affecting the assembly of the Lhca1-Lhca4 heterodimer of the canonical LHCI belt. Indeed, residues mediating interactions between Lhca1-Lhca4 and the core differ in Lhca1$_5$-Lhca4$_6$, allowing relatively unrestricted mutation for building the docking sites. The LHCII N-terminus phosphosite anchors docking to PSI, as in ST2 of land plants. However, rather than being part of a rapidly reversible acclimatory process shuttling LHCII between PSI and PSII, to balance preferential excitation (Fig. 1d), LHCII remains phosphorylated even after prolonged dark adaptation. It remains unclear why the full assembly of PSI-LHCI-mega is limited to a PSI-LHCI-mega/PSI-LHCI ratio of ~0.3 (Supplementary Fig. 2c), while photon harvesting limitation increases with depth. PSI-LHCI-mega assembly may occur cooperatively through multiple component interactions and may depend on the chloroplastic kinase/phosphatase system activity[46]. This process is regulated by the redox state of the plastoquinone pool, which in turn is influenced by depth-dependent spectrally distinct light conditions, thereby affecting the PSI *vs.* PSII activities. The homeostatic balance between ST1-2 under dim light at depth may maintain the system in an intermediate state[23]. As for the activity of the LHCII phosphatase, presumably PPH1[46], it is likely to have a peculiar regulation since LHCII connected to PSI-LHCI remains fully phosphorylated during the long procedure of sampling and transportation of leaves in the dark, before thylakoid extraction, a time-lapse that causes complete dephosphorylation in land plants[47]. Instead, the phosphorylated LHCII reactivity was barely detectable in the main LHCII fraction (B3; Fig. 1e, Supplementary Fig. 3f), suggesting an active LHCII phosphatase in *P. oceanica* chloroplasts. Analysis of the *P. oceanica* genome and transcriptome identified homologs for STN7 (*POSOC 04g00070 92% identity)*, STN8 (*Posoc01g27130 64% identity*), PPH1/TAP38 *(Posoc01g37740, Posoc03g20940*), with decreased identity levels (55-65%). Although functional domains appear conserved, the reduced identity, especially in phosphatases, suggests significant differences in the regulation of catalytic activities. Indeed, unlike land plants, the fast-reversible phosphorylation activity is very low (Supplementary Fig. 2d, 3f), whereas LHCII binding to PSI-LHCI-mega (Supplementary Fig. 2c) appears to be a constitutive adaptation strategy. This hypothesis is supported by the observation of a green band containing a PSI-LHCI-mega-like complex from an *A. thaliana pph1* mutant[48].

In conclusion, we have characterized *P. oceanica* PSI supercomplexes, revealing key adaptations to the low-intensity, blue-shifted light of the seabed. These adaptations include: *a*) the enhancement of Chl *b* content in Lhc proteins (Supplementary Fig. 3a, b), increasing blue light absorption due to different extinction of Chl *a vs.* Chl *b* in the Q$_y$ *vs.* Soret spectral ranges; *b*) the enhancement of both photosystems functional cross-section (Fig. 1b, c) for photon harvesting. Trapping time inversely correlates with quantum efficiency in photosynthetic systems[11], implying that an increase in antenna size could be detrimental for light-use efficiency under dim light. Consistently, the low-energy Chl forms that slow PSI trapping time[38,40], have been lost in *P. oceanica* LHCI, representing an adaptation that enhances EET

dynamics within the PSI while concurrently preserving high quantum yield and overall light-use efficiency despite the enlarged antenna system (Fig. 5); *c*) PSI antenna expansion achieved both by duplicating an LHCI heterodimer into an alternative docking site and by permanently incorporating trimeric phosphorylated-LHCII into the PSI-LHCI-mega through a phosphorylation-dependent mechanism already active in land plants.

Besides revealing the molecular strategies underlying seagrass adaptation to the marine environment, these findings open avenues for crop engineering: introducing *P. oceanica*-like PSI-mega complexes and tuning far-red absorption could boost PSI activity, enhancing photosynthesis under shaded canopy conditions[9,49].

Methods

Plant collection

Posidonia oceanica orthotropic shoots, holding rhizome and roots, were collected by hand-picking SCUBA diving at 22 and 4 mt, near Lacco Ameno, Ischia Island, Naples, Italy. Both depths were sampled on the same day in successive dives. Sampling was carried out in July and October 2024. Once collected, the plants were kept in seawater and darkness, and then quickly transported to the laboratory for processing and analysis. Leaves were separated from the rhizome and bundles under green light, and epiphytic organisms were removed by washing with seawater and gentle scraping. *Arabidopsis thaliana* (WT *Col*-0) and *Zea mays* (WT) plants were grown for 6 weeks and 8–9 weeks, respectively, under 150 μmol photons m^{-2} s^{-1}, 23 °C, 70% relative humidity, and an 8/16 h light/dark photoperiod.

Thylakoid membranes isolation

Thylakoid membranes were isolated as previously described in ref. 22. Briefly, dark-adapted leaves were homogenized in grinding buffer containing 20 mM Tricine (pH 7.8), 300 mM sorbitol, 10 mM EDTA, 10 mM $NaHCO_3$, 0.15% BSA, 5% polyethylene glycol 4000, and 5% ascorbic acid. The homogenate was filtered through nylon tissue (20–25 μm) to remove debris and unbroken cells. The filtrate was centrifuged at 2500 × *g* for 15 min at 4 °C, and the resulting pellet was resuspended in hypotonic buffer (25 mM Hepes-KOH pH 7.5, 25 mM sorbitol, 5 mM NaCl, 5 mM $MgCl_2$, 5 mM KCl) to lyse chloroplasts. After low-speed centrifugation (100 × *g* for 2 min at 4 °C) to remove large particles, the supernatant was transferred to a new tube and centrifuged at 3500 × *g* for 10 min at 4 °C. The resulting pellet, enriched in thylakoid membranes, was gently resuspended in storage buffer (50 mM Hepes pH 7.5, 300 mM sorbitol, 10 mM NaCl, 5 mM $MgCl_2$). Protease inhibitors (5 mM benzamidine and 5 mM caproic acid) and 10 mM NaF were added to all pre-cooled buffers at 4 °C immediately before use.

Analysis of chlorophyll fluorescence

Chlorophyll fluorescence parameters, including Fv/Fm, ETR-II, ST1-2 transitions, and NPQ, were measured on intact leaves using a DUAL-PAM-100.

Time-resolved fluorescence measurements were performed on recombinant proteins using a time-correlated single-photon counting (TCSPC) setup. Samples were excited at 440 nm using a picosecond-pulsed diode laser operating at 40 MHz. Fluorescence emission was collected through a 650 nm long-pass filter and detected by a single-photon avalanche diode (SPAD) connected to a TCSPC module. The overall instrumental response function was approximately 80 ps (FWHM). Samples were diluted to an optical density of 0.1 cm^{-1} at the Qy maximum and measured at room temperature. Fluorescence decay traces were fitted in MATLAB.

Functional cross-section of photosystems

Functional PSII cross-section was determined on thylakoid membranes using a custom-built setup, applying 7 μmol photons m^{-2} s^{-1} of green light in a buffer containing 20 mM Hepes (pH 7.0), 150 mM sorbitol, and 50 μM DCMU. Functional PSI cross-section size was measured using a Joliot-Type Spectrophotometer (JTS-10, Biologic), monitoring absorption changes at 705 nm in thylakoid membranes (50 μg Chl/mL) suspended in a buffer containing 0.4 M sorbitol, 15 mM NaCl, 5 mM $MgCl_2$, 10 mM Hepes (pH 7.5), 50 μM DCMU, 100 μM methylviologen, and 500 μM sodium ascorbate. The two-thirds rise time of fluorescence (PSII) or oxidation (PSI) was used to estimate the functional cross-section of each photosystem.

Purification of photosynthetic complexes

Thylakoid membranes from *P. oceanica*, *A. thaliana*, and *Z. mays* were adjusted to a chlorophyll concentration of 1 mg/mL in 10 mM Hepes (pH 7.5), 20 mM EDTA, 10 mM NaF, and solubilized by adding an equal volume of 2% n-dodecyl-β-D-maltopyranoside (β-DM, w/v). Samples were incubated on ice for 15 min, and insoluble material was removed by centrifugation at 12,000 × *g* for 15 min at 4 °C. The supernatant was loaded on a 0.1–1.3 M sucrose gradient (10 mM Hepes pH 7.5, 0.015% β-DM) and fractionated by ultracentrifugation at 141,000 × *g* for 36 h at 4 °C (Beckman SW28 Ti). Distinct bands were collected using a Hamilton syringe.

Gel electrophoresis and immunoblotting

SDS-PAGE was carried out using the Tris-Tricine buffer system, and gels were stained with Coomassie Brilliant Blue R250. For immunoblotting, proteins were electroblotted onto nitrocellulose membranes and probed with the following primary antibodies: α-Lhca1 (Agrisera AS01005), α-Lhca2 (AS01006), α-Lhca3 (AS01007), α-Lhca4 (AS01008), α-Lhcb1 (AS01004), α-Lhcb2 (AS01003), phosphorylated α-Lhcb2 (AS132705), and α-PsaA (AS06172). Non-denaturing Deriphat-PAGE and large-pore Blue Native gels were carried out according to refs. 50,51.

Pigments analysis

Pigments were extracted from isolated complexes using 80% acetone buffered with Na_2CO_3, and subsequently separated and quantified either by HPLC or by fitting the acetone extract spectrum as described in refs. 52.

Steady-state spectroscopy

Absorption spectra were recorded at room temperature using a SHIMADZU 2700i spectrophotometer in a buffer containing 10 mM Hepes (pH 7.5) and 0.015% β-DDM. Fluorescence emission spectra were recorded at 77 K using an Ocean Insight SR-6NVN500-50 spectrofluorometer. Excitation was provided by a white light source filtered through a 448 nm short-pass filter, and samples were diluted in a buffer containing 10 mM Hepes (pH 7.5), 0.015% β-DM, and 0.3 M sucrose. Circular dichroism spectra were recorded at 4 °C using a Jasco J-1500 spectropolarimeter.

Amino acid sequences of *P. oceanica*

The LHC and core amino acid sequences shown in Supplementary Fig. 26 and used for Cryo-EM structural model reconstruction were derived from ref. 6. To validate these sequences, a bidirectional ortholog analysis was also performed with orthologs from *A. thaliana* and *Z. mays*. Functional domains similarity analysis was performed with InterPro (https://www.ebi.ac.uk/interpro/).

Expression and reconstitution of recombinant proteins

Wild-type and mutant sequences of *P. oceanica* Lhca4 containing a C-terminal 8 × His-tag were purchased as synthetic genes (www.eurofins.com) and cloned into *E. coli* BL21 strain, for apoprotein expression. Synthetic genes are provided in the Source Data. Reconstitution and purification of pigment-protein complexes were performed as described in Ref. 25. Briefly, proteins were reconstituted

with pigments to their native state[25] and subsequently purified using IMAC chromatography and sucrose density gradient ultracentrifugation (Supplementary Fig. 25a, b).

Statistical analysis

Statistical analyses were performed using one-way analysis of variance (ANOVA) followed by Tukey's post hoc test. *P*-values are indicated in the figure legends. Error bars represent standard deviation, and means not sharing the same lower-case letters are considered significantly different.

Cryo-EM sample preparation and vitrification

For Cryo-EM preparations, *P. oceanica* PSI-LHCI (B6) and PSI-LHCI-mega (B7) samples were washed with a 10 mM Hepes (pH 7.5) and 0.015% β-DM solution and concentrated to 1 mg/mL Chls with 100 kDa Vivaspin 20 concentrators (Sartorius). Samples were prepared following a standardized cryopreservation procedure to ensure optimal image quality during Cryo-EM data acquisition. The particle-containing solutions were centrifuged at 15,000 rpm at 4 °C for 15 min to remove potential aggregates or debris. Subsequently, 3 µL aliquots of each sample, at a final concentration of approximately 1 mg/mL of Chl, were applied to 300-mesh Ultrafoil gold grids with 1.2 µm hole size, previously treated by glow discharge to enhance sample adherence. Vitrification was performed using a Vitrobot Mark IV (Thermo Fisher) operating at 4 °C and 100% relative humidity. After the sample application, the grids were blotted for 5 s to remove excess solution and then rapidly plunged into liquid ethane cooled by liquid nitrogen, ensuring fast vitrification and preventing ice crystallization. The frozen grids were then transferred and stored in liquid nitrogen until data acquisition.

Cryo-EM data acquisition

Cryo-EM images were acquired using a Glacios transmission electron microscope (TEM) (Thermo Fisher) operating at 200 kV, equipped with a Falcon 4i Direct Electron Detector (Thermo Fisher) for data collection. Images were recorded at a nominal magnification of 130,000X, corresponding to a pixel size of 0.92 Å. To enhance contrast and optimize image quality, the defocus was set within a range of −0.75 µm to −2.5 µm, with increments of 250 nm. An energy filter with a width of 10 eV was applied to reduce noise from inelastic electrons. The total exposure applied during acquisition was approximately 50 e −/Å², divided into 40 frames to minimize sample movement artifacts. A total of 6132 and 1453 movies were collected for the B7 and B6 samples, respectively.

Cryo-EM data processing and image reconstruction

All image processing and reconstruction steps were performed using CryoSPARC v4.6.2[53]. The experimental workflows are outlined in Supplementary Figs. 4, 5. For B7, after patch motion correction and CTF estimation, a first dataset of 3476 manually curated exposures was used for the initial particle picking. After an initial round of reference-free autopicking on a subset of micrographs and 2D classification, the best 2D classes were used for template-based autopicking on the whole dataset. Particles were extracted with a box size of 400 pixels (px), binned 2 × 2, and subjected to multiple rounds of 2D classification. The best 2D classes, consisting of 211,443 particles (ptcs), were used for ab-initio reconstruction (3 classes) and heterogeneous refinement. The particles corresponding to PSI-LHCI supercomplexes, re-extracted at full size, were subjected to homogeneous refinement and subsequently to 3D classification in order to separate subsets corresponding to PSI-LHCI-mega (Class 3, 24,916 ptcs) and PSI-LHCI supercomplexes (Classes 4 and 5, 66,715 ptcs). A second dataset of 2656 movies was processed in a similar way, and the particles of the 3D class corresponding to PSI-LHCI-mega (Class 3b, 12,851 ptcs) were merged with those of the first dataset (Class 3). These particles were re-extracted at full resolution (400 pixel box size) and subjected to global and local CTF refinement and reference-based motion correction (RBMC). Following a final round of non-uniform refinement, a final consensus map with a resolution of 3.31 Å was obtained with a total of 37,162 ptcs. Three soft-edged masks covering the PSI core, LHCI belt, and Lhca1$_5$-4$_6$ extra heterodimer-LHCII trimer were generated with USCF ChimeraX and imported into CryoSPARC. Local refinement for the PSI core and LHCI belt provided maps with resolutions of 3.23 and 3.50 Å, respectively. For the Lhca1$_5$-Lhca4$_6$-LHCII trimer, additional focused 3-D classification was used to isolate a subset of 22,405 particles in which the LHCII trimer was clearly visible, which was used for the final local refinement to produce a map with 3.63 Å resolution. In all maps, the resolution was estimated by the "gold-standard" Fourier Shell Correlation (FSC = 0.143) criterion. The data for generating the FSC curves and three-dimensional orientation distribution plots were exported from CryoSPARC (Supplementary Fig. 6a, b, d, e). Local resolution estimation was performed as implemented in CryoSPARC on the unsharpened maps (Supplementary Fig. 6c, f). The consensus map and the three local maps were sharpened and used to generate a combined map with the Combine Focused Maps tool in Phenix v.1.21[54]. For B6, a total of 1453 manually curated exposures were used for particle picking and 2D classification. 2D classes corresponding to different views of PSI-LHCI of the B7 dataset were used for initial template-based autopicking, resulting in an initial stack of 184,021 particles. After two rounds of 2D classification, a total of 92,897 particles were used to obtain an initial reconstruction of the PSI-LHCI complex at 4.55 Å resolution. After re-extraction at full resolution (400 pixel box size), 3D classification was used to isolate a subset of 54,305 high-quality particles (Class 1 and 2 in Supplementary Fig. 5). This stack was merged with particles from 3D classes 4 and 5 of B7 first dataset and subjected to global and local CTF refinement, RBMC and non-uniform refinement, yielding a consensus map with a resolution of 2.83 Å (120,603 ptcs). Local refinement with masks for the PSI core and LHCI belt produced maps with resolutions of 2.79 Å and 3.06 Å, respectively (Supplementary Fig. 5). After sharpening, the consensus and local maps were combined as described above.

Model building and refinement

The structure of maize PSI-LHCI-LHCII supercomplex (PDB code 5ZJI[31]) was used as the starting model. For *P. oceanica* PSI-LHCI, after initial docking of the starting model (without the LHCII trimer) in the composite map with USCF ChimeraX, each protein chain was independently rigid-body fitted and refined with Phenix-refine[55]. The amino acid sequences of the different subunits were manually mutated to match the sequences of *P. oceanica* (Supplementary Fig. 26) using COOT[56], and the resulting model underwent several rounds of real-space refinement (with geometry and secondary structure restraints) in Phenix and manual rebuilding in COOT. Ligand restraints for refinement were generated with eLBOW or with the Grade2 web server (https://grade.globalphasing.org). For PSI-LHCI-mega, the refined model of *P. oceanica* PSI-LHCI was first docked into the map, followed by fitting the models of PsaO, LHCII trimer, and Lhca1$_5$-Lhca4$_6$ dimer in the corresponding densities to generate an initial model of the supercomplex. After introducing the correct side chains to match the protein sequences of *P. oceanica* (Supplementary Fig. 26)[6], the model was subjected to cycles of real-space refinement and manual reconstruction in COOT. Because the density in this part of the map did not allow unambiguous identification of the different subunits of the LHCII trimer, this was modeled with one Lhcb2 (identified by the presence of the phosphorylated threonine 39) and two Lhcb1 subunits. The FSC curves between the models and the composite Cryo-EM density maps (Supplementary Figs. 7a, 10a) were calculated with phenix.mtriage[55]. The stereochemical quality of the final models was assessed with MolProbity[57]. Data collection and model refinement statistics are summarized in Supplementary Table 5. High-resolution figures were prepared with ChimeraX and PyMOL.

Reporting summary

Further information on research design is available in the Nature Portfolio Reporting Summary linked to this article.

Data availability

The composite cryo-EM maps of the *P. oceanica* PSI-LHCI and L-PSI-LHCI-LHCII (PSI-LHCI-mega) and the corresponding atomic coordinates generated in this study have been deposited in the Electron Microscopy Data Bank and the Protein Data Bank under the accession codes of EMD-54455 and 9S1L for PSI-LHCI, and EMD-54456 and 9S1M for PSI-LHCI-mega. The PSI-LHCI focused map with a better density of PSI core and LHCI belt has been deposited in the Electron Microscopy Data Bank under accession codes EMD-54380 and EMD-54396, respectively. The consensus map of PSI-LHCI has been deposited in the Electron Microscopy Data Bank with accession code EMD-54379. The PSI-LHCI-mega focused map, with a better density of the PSI core, LHCI belt, and Lhca1$_5$-4$_6$-LHCII, has been deposited in the Electron Microscopy Data Bank with accession codes EMD-54441, EMD-54443 and EMD-54444, respectively. The consensus map of PSI-LHCI-mega has been deposited in the Electron Microscopy Data Bank with accession code EMD-54439. All data analyzed during this study are included in this article and its Supplementary Information. Additional related data and materials are available in the Source Data file or from the corresponding authors upon request. Source data are provided with this paper.

References

1. Le Hir, G. et al. The climate change caused by the land plant invasion in the Devonian. *Earth Planet. Sci. Lett.* **310**, 203–212 (2011).
2. Duarte, C. M., Middelburg, J. J. & Caraco, N. Major role of marine vegetation on the oceanic carbon cycle. *Biogeosciences* **2**, 1–8 (2005).
3. Ott, J. A. Growth and production in *Posidonia oceanica* (L.) Delile. *Mar. Ecol.* **1**, 47–64 (1980).
4. Larkum, A. W. D. et al. *Photosynthesis and Metabolism of Seagrasses*. (Springer, 2018).
5. Fourqurean, J. W. et al. Seagrass ecosystems are a globally significant carbon stock. *Nat. Geosci.* **5**, 505–509 (2012).
6. Ma, X. et al. Seagrass genomes reveal ancient polyploidy and adaptations to the marine environment. *Nat. Plants* **10**, 240–255 (2024).
7. Ritchie, R. J., Larkum, A. W. D. & Ribas, I. Could photosynthesis function on Proxima Centauri b?. *Int. J. Astrobiol.* **17**, 147–176 (2018).
8. Ecol, M. et al. Light gradients and meadow structure in Posidonia oceanica: ecomorphological and functional correlates. *Mar. Ecol. Prog. Ser.* **163**, 267–278 (1998).
9. Amelii, A. et al. Photosynthesis under far-red light—evolutionary adaptations and bioengineering of light-harvesting complexes. *FEBS Lett.* **600**, 164–187 (2025).
10. Nelson, N. & Junge, W. Structure and energy transfer in photosystems of oxygenic photosynthesis. *Annu. Rev. Biochem.* **84**, 659–683 (2015).
11. Croce, R. & van Amerongen, H. Light harvesting in oxygenic photosynthesis: structural biology meets spectroscopy. *Science* **369**, eaay2058 (2020).
12. Croce, R. & Van Amerongen, H. Natural strategies for photosynthetic light harvesting. *Nat. Chem. Biol.* **10**, 492–501 (2014).
13. Pan, X., Cao, P., Su, X., Liu, Z. & Li, M. Structural analysis and comparison of light-harvesting complexes I and II. *Biophys. Acta Bioenerg.* **1861**, 148038 (2020).
14. Huang, Z. et al. Structure of photosystem I-LHCI-LHCII from the green alga Chlamydomonas reinhardtii in State 2. *Nat. Commun.* **11**, 1100 (2021).
15. Shen, L. et al. Structure and function of a huge photosystem I–fucoxanthin chlorophyll supercomplex from a coccolithophore. *Science* **389**, eadv2132 (2025).
16. Li, X. et al. Structures and organizations of PSI–AcpPCI supercomplexes from red tidal and coral symbiotic photosynthetic dinoflagellates. *Proc. Natl. Acad. Sci. USA* **121**, e2315476121 (2024).
17. Telesca, L. et al. Seagrass meadows (*Posidonia oceanica*) distribution and trajectories of change. *Sci. Rep.* **5**, 12505 (2015).
18. Arnaud-Haond, S. et al. Implications of extreme life span in clonal organisms: millenary clones in meadows of the threatened seagrass Posidonia oceanica. *PLoS ONE* **7**, e30454 (2012).
19. Pergent-Martini, C. et al. Contribution of *Posidonia oceanica* meadows in the context of climate change mitigation in the Mediterranean Sea. *Mar. Environ. Res.* **165**, 105236 (2021).
20. Procaccini, G. et al. Depth-specific fluctuations of gene expression and protein abundance modulate the photophysiology in the seagrass *Posidonia oceanica*. *Sci. Rep.* **7**, 42890 (2017).
21. Ferroussier, Q. C. et al. Thriving across seawater depths: how blue light shapes a large PSI supercomplex and specific photosynthetic traits in the seagrass Posidonia oceanica. *Plant Commun.* **7**, 101574 (2025).
22. Charras, Q. et al. An efficient protocol for extracting thylakoid membranes and total leaf proteins from Posidonia oceanica and other polyphenol-rich plants. *Plant Methods* **20**, 38 (2024).
23. Goldschmidt-Clermont, M. & Bassi, R. Sharing light between two photosystems: mechanism of state transitions. *Curr. Opin. Plant Biol.* **25**, 71–78 (2015).
24. Cazzaniga, S., Bressan, M., Carbonera, D., Agostini, A. & Dall'Osto, L. Differential roles of carotenes and xanthophylls in photosystem I photoprotection. *Biochemistry* **55**, 3636–3649 (2016).
25. Morosinotto, T., Breton, J., Bassi, R. & Croce, R. The nature of a chlorophyll ligand in Lhca proteins determines the far red fluorescence emission typical of photosystem I. *J. Biol. Chem.* **278**, 49223–49229 (2003).
26. Capaldi, S. et al. Structural determinants for red-shifted absorption in higher-plants Photosystem I. *N. Phytol.* **248**, 2331–2346 (2025).
27. Ben-Shem, A., Frolow, F. & Nelson, N. Crystal structure of plant photosystem I. *Nature* **426**, 630–635 (2003).
28. Qin, X., Suga, M., Kuang, T. & Shen, J.-R. Structural basis for energy transfer pathways in the plant PSI-LHCI supercomplex. *Science* **16**, 989–995 (2015). *348*.
29. Li, X. et al. Structure of the red-shifted Fittonia albivenis photosystem I. *Nat. Commun.* **15**, 6325 (2024).
30. Mazor, Y., Borovikova, A., Caspy, I. & Nelson, N. Structure of the plant photosystem I supercomplex at 2.6 Å resolution. *Nat. Plants* **3**, 17014 (2017).
31. Pan, X. et al. Structure of the maize photosystem I supercomplex with light-harvesting complexes I and II. *Science* **360**, 1109–1113 (2018).
32. Wu, J. et al. Regulatory dynamics of the higher-plant PSI–LHCI supercomplex during state transitions. *Mol. Plant* **16**, 1937–1950 (2023).
33. Galka, P. et al. Functional analyses of the plant photosystem I-light-harvesting complex II supercomplex reveal that light-harvesting complex II loosely bound to photosystem II is a very efficient antenna for photosystem I in state II. *Plant Cell* **24**, 2963–2978 (2012).
34. Longoni, P., Douchi, D., Cariti, F., Fucile, G. & Goldschmidt-Clermont, M. Phosphorylation of the light-harvesting complex II isoform Lhcb2 is central to state transitions. *Plant Physiol.* **169**, 2874–2883 (2015).
35. Zhang, S. et al. Structural insights into a unique PSI–LHCI–LHCII–Lhcb9 supercomplex from moss *Physcomitrium patens*. *Nat. Plants* **9**, 832–846 (2023).

36. Mukamel, S. Multidimensional femtosecond correlation spectroscopies of electronic and vibrational excitations. *Annu. Rev. Phys. Chem.* **51**, 691–729 (2000).
37. Brixner, T. et al. Two-dimensional spectroscopy of electronic couplings in photosynthesis. *Nature* **434**, 625–628 (2005).
38. Russo, M., Casazza, A. P., Cerullo, G., Santabarbara, S. & Maiuri, M. Direct evidence for excitation energy transfer limitations imposed by low-energy chlorophylls in photosystem I-light harvesting complex I of land plants. *J. Phys. Chem. B* **125**, 3566–3573 (2021).
39. Le Quiniou, C. et al. PSI-LHCI of *Chlamydomonas reinhardtii*: Increasing the absorption cross-section without losing efficiency. *Biochim. Biophys. Acta Bioenerg.* **1847**, 458–467 (2015).
40. Engelmann, E. et al. Influence of the photosystem I-light harvesting complex I antenna domains on fluorescence decay. *Biochemistry* **45**, 6947–6955 (2006).
41. Romero, E. et al. The origin of the low-energy form of photosystem I light-harvesting complex Lhca4: mixing of the lowest exciton with a charge-transfer state. *Biophys. J.* **96**, L35–L37 (2009).
42. Sláma, V. et al. Origin of low-lying red states in the Lhca4 light-harvesting complex of photosystem I. *J. Phys. Chem. Lett.* **14**, 8345–8352 (2023).
43. Wientjes, E., Roest, G. & Croce, R. From red to blue to far-red in Lhca4: How does the protein modulate the spectral properties of the pigments?. *Biochim. Biophys. Acta Bioenerg.* **1817**, 711–717 (2012).
44. Li, X. et al. LHCA4 residues surrounding red chlorophylls allow for fine-tuning of the spectral region for photosynthesis in Arabidopsis thaliana. *Front. Plant Sci.* **13**, 1118189 (2023).
45. Hendriks, I. E., Olsen, Y. S. & Duarte, C. M. Light availability and temperature, not increased CO2, will structure future meadows of *Posidonia oceanica*. *Aquat. Bot.* **139**, 32–36 (2017).
46. Shapiguzov, A. et al. The PPH1 phosphatase is specifically involved in LHCII dephosphorylation and state transitions in Arabidopsis. *Proc. Natl. Acad. Sci. Usa.* **107**, 4782–4787 (2010).
47. Samol, I. et al. Identification of a photosystem II phosphatase involved in light acclimation in Arabidopsis. *Plant Cell* **24**, 2596–2609 (2012).
48. Crepin, A., Kučerová, Z., Kosta, A., Durand, E. & Caffarri, S. Isolation and characterization of a large photosystem I–light-harvesting complex II supercomplex with an additional Lhca1–a4 dimer in Arabidopsis. *Plant J.* **102**, 398–409 (2020).
49. Wang, Y., Oliver, T. J., Croce, R. & Long, S. P. Addition of longer wavelength absorbing chlorophylls into crops could increase their photosynthetic productivity by 26%. *Nat. Commun.* **16**, 7933 (2025).
50. Havaux, M., Dall'Osto, L., Cuiné, S., Giuliano, G. & Bassi, R. The effect of zeaxanthin as the only xanthophyll on the structure and function of the photosynthetic apparatus in *Arabidopsis thaliana*. *J. Biol. Chem.* **279**, 13878–13888 (2004).
51. Järvi, S., Suorsa, M., Paakkarinen, V. & Aro, E. M. Optimized native gel systems for separation of thylakoid protein complexes: novel super- and mega-complexes. *Biochem. J.* **439**, 207–214 (2011).
52. Chazaux, M., Schiphorst, C., Lazzari, G. & Caffarri, S. Precise estimation of chlorophyll a, b and carotenoid content by deconvolution of the absorption spectrum and new simultaneous equations for Chl determination. *Plant J.* **109**, 1630–1648 (2022).
53. Punjani, A., Rubinstein, J. L., Fleet, D. J. & Brubaker, M. A. CryoSPARC: Algorithms for rapid unsupervised cryo-EM structure determination. *Nat. Methods* **14**, 290–296 (2017).
54. Liebschner, D. et al. Macromolecular structure determination using X-rays, neutrons and electrons: recent developments in Phenix. *Acta Crystallogr. D. Struct. Biol.* **75**, 861–877 (2019).
55. Afonine, P. V. et al. Towards automated crystallographic structure refinement with phenix.refine. *Acta Crystallogr. D. Biol. Crystallogr.* **68**, 352–367 (2012).
56. Emsley, P., Lohkamp, B., Scott, W. G. & Cowtan, K. Features and development of Coot. *Acta Crystallogr. D. Biol. Crystallogr.* **66**, 486–501 (2010).
57. Chen, V. B. et al. MolProbity: All-atom structure validation for macromolecular crystallography. *Acta Crystallogr. D. Biol. Crystallogr.* **66**, 12–21 (2010).
58. Sardar, S. et al. Revealing molecular mechanisms of photosynthetic light harvesting with ultrafast optical spectroscopy. *J. Phys. Photonics* **8**, 012002 (2026).

Acknowledgments

We thank the Center for Technological Platforms (CPT, https://cpt.univr.it/) of the University of Verona for access to spectroscopy, diffractometry, and molecular interaction facilities. We also thank Daniele Montepietra for site-energy rescaled FRET-EET rate calculations, Fabio Blanco Murillo and Bruno Iacono (RIMAR, Stazione Zoologica Anton Dohrn Napoli) for assistance with sampling, and Jessica Pazzaglia and Emanuela Dattolo for logistical support and discussions on ecological and evolutionary implications.

Author contributions

R.B., A.A., G.P., L.D. and S.C. conceived and coordinated the project. A.A., I.O. and G.P. performed plant harvesting and thylakoid membrane preparation. A.A. and Z.G. performed the physiological characterization. A.A., S.C. and Z.G. performed the biochemical and spectroscopic analyses. A.A. purified and prepared PSI supercomplexes for Cryo-EM analysis and ultrafast spectroscopy. E.E. and G.S. performed Cryo-EM sample preparation and data collection. S.C. analyzed Cryo-EM data, built and refined the structural model. M.R., M.M. and G.C. performed the ultrafast measurements and analyzed the data. A.A., S.C., M.R., G.C. and R.B. wrote the original manuscript draft, with all authors contributing to result discussions and manuscript revisions.

Funding

This work was funded by the European Research Council (ERC) Advanced Grant (101053983- GrInSun) to R.B. and L.D.; the European Marine Biological Resource Center (EMBRC-IT) Grant (3097-PhotoSEA) to A.A.; European Innovation Council PLANKT-ON, Plankton-Like Protocelles for Artificial Photosynthesis Targeting Carbon-Neutral Energy Vectors, Pathfinder-Open 2022 (Grant Agreement N. 101099192) to M.R. and M.M.; and PON IMPARA PIR01_0023 to Cryo-electron microscopy, "EYE LAB" laboratory, ISASI-CNR, Naples.

Competing interests

The authors declare no competing interests.

Additional information

Supplementary information The online version contains supplementary material available at https://doi.org/10.1038/s41467-026-75200-8.

Correspondence and requests for materials should be addressed to Roberto Bassi.

Peer review information *Nature Communications* thanks Senfang Sui, who co-reviewed with Guogiang Huang and Dvir Harris for their contribution to the peer review of this work. A peer review file is available.